Journal Name

COMMUNICATION

Supporting Information

Pseudocapacitance contribution in boron-doped graphite sheets for anion storage enables high-performance sodium-ion capacitors

Feng Yu,[a‡] Zaichun Liu,[c‡] Renwu Zhou,[a‡] Deming Tan,[b] Hongxia Wang,*[a] Faxing Wang*[b]

[a.] School of Chemistry, Physics and Mechanical Engineering, Science and Engineering Faculty, Queensland University of Technology, Brisbane, Australia. Email: hx.wang@qut.edu.au
[b.] Department of Chemistry and Food Chemistry, Technische Universität Dresden, 01062 Dresden, Germany. Email: faxing.wang@tu-dresden.de.
[c.] School of Energy Science and Engineering, and Institute for Advanced Materials, Nanjing Tech University, Nanjing, China.

‡These authors equally contributed to this work.

Experimental Section

Preparation of B-doped graphite nanosheets. Graphite nanosheets were obtained by exfoliating the graphite foil according to the electrochemical expansion method reported previously with minor modifications.[1] A two-electrode cell was fabricated using aqueous NH_4NO_3 (0.1 M) as the electrolyte and graphite foils as both the negative and positive electrodes at 10 V for 3 min. Subsequently, the negative and positive electrodes were changed under the same voltage for an additional 3 min. This process was alternated until the peeling of both the positive and negative electrodes was completed. The obtained graphite nanosheets were washed several times with deionized water to remove chemical residues. To B-doped graphite nanosheets, the 40 ml graphite aqueous dispersion and 5 mmol ammonia boric acid (H_3BO_3) were mixed through sonication for 15 min. The resulting stable suspension was then sealed in a Telfon-lined autoclave and heated to react at 180°C for 24 h. Finally, the as-prepared sample was washed several times with deionized water and ethanol and freeze-dried overnight.

Preparation of hollow carbon nanospheres. The SiO_2 microsphere and resorcinol/formaldehyde (RF) were employed as hard template and carbon precursor, respectively. The SiO_2 microspheres with a uniform diameter of ~100 nm were first prepared through the Stöber process.[2] Then, the core-shell structured RF enwrapped SiO_2 microspheres (SiO_2@RF) was prepared by a facile silica-assisted sol-gel coating process.[2,3] After carbonization at 600 ^oC under N_2 atmosphere and subsequently etching of SiO_2 by NaOH aqueous solution, the as-made SiO_2@RF microspheres were converted into hollow graphitized carbon nanospheres.

Characterizations. SEM imaging and energy dispersive X-ray spectroscopy were performed using a field emission scanning electron microscope (Carl Zeiss NVision 40, integrated with an EDAX system) at an acceleration voltage of 10.0 kV. TEM was performed using a JEOL JEM-2010 transmission electron microscope. AFM images were obtained using a nanoscope (Veeco Instruments Inc.) in the tapping mode. Surface chemical states of materials were investigated by X-ray photoelectron spectroscopy (XPS; Perkin-Elmer PHI 5000C ESCA, using Al KR radiation). For the electrode tests when charged to 4 V, the BG electrode after was taken out of the hybrid device in glove box were rinsed with anhydrous DMC to remove the electrolyte, then were washed with acetone and dried overnight. For the *in situ*

electrochemical-Raman measurements, a simulated thin film battery was used in which the BG and HC was used as the positive and negative electrodes in 1 M $NaPF_6$ in ethylene carbonate/dimethyl carbonate (EC/DMC, 6:4, v/v) electrolyte. There is a pore on the side of BG electrode sealed by transparent plastic. Raman spectra (1480–1680 cm^{-1}) were obtained on a custom-made confocal Raman spectrometer (Ntegra Aura/Spectra) from NT-MDT (Moscow, Russia) using a HeNe laser (532 nm) with 2 cm^{-1} resolution.

Electrochemical measurements. The working electrode was prepared by coating the N-methyl-2-pyrrolidone-based slurry containing BG (or HC) powder, acetylene black, and PVDF in a weight ratio of 8:1:1 on current collectors by using a doctor blade technique. The coated foils were dried and punched into circular shapes (d = 11 mm), which were further dried at 100 °C for 12 h under vacuum. The area of the electrode was 0.95 cm^2. The loading densities of the BG and HC electrode were 1.5 mg cm^{-2} and 1.2 mg cm^{-2}, respectively. For the cathode, the current density of 0.5 A g^{-1} corresponds to about 0.75 mA cm^{-2}. For the anode, the current density of 0.5 A g^{-1} corresponds to about 0.6 mA cm^{-2}. A Celgard 2730 membrane and 1 M $NaPF_6$ in ethylene carbonate/dimethyl carbonate (EC/DMC, 6:4, v/v) were used as the separator and the electrolyte, respectively. All cells were assembled in an Ar-filled glove box with O_2 and H_2O content below 0.1 ppm. Half cells were constructed using coin-type 2032 model cells, with Na metal as the counter and reference electrodes. When constructing the full cell to attain a highly efficient Na-ion hybrid capacitor, a mass balance between the negative and positive electrodes was optimized according to the following equation of $Q_+ = Q_- = m_+V_+ C_+ = m_- V_- C_-$, where m, V and C are the mass of active electrode, the potential range and capacitance, respectively, and subscripts stand for the positive and negative electrode, respectively. Electrochemical measurements of the Na-ion hybrid capacitor were conducted using two-electrode cells at room temperature. Cyclic voltammetry (CV) and galvanostatic charge-discharge curves were obtained using an electrochemical station (CHI660B) and a Land battery testing system, respectively. For the Na ion hybrid capacitor, the specific capacitance, energy density and power density (P) were calculated based on the total mass of the active materials from the positive and negative electrode. All the electrochemical measurements were performed at room temperature. The energy (E) and power (P) densities of the Na ion capacitors were calculated by numerically integrating the galvanostatic discharge profiles using the following equations, [4,5]

$$E = \int_{t1}^{t2} IV dt = \Delta V \times \frac{I}{m} \times t \qquad (S1)$$

$$\Delta V = \frac{Vmax + Vmin}{2} \quad (S2)$$

$$P = \frac{E}{t} = \Delta V \times \frac{I}{m} \quad (S3)$$

where t is the discharge time (s), $\frac{I}{m}$ is the constant current density (A g^{-1}), V_{max} is the voltage (V) at the beginning of discharge after the IR drop, and V_{min} is the voltage (V) at the end of discharge.

Theoretical calculations. All calculations reported herein were performed using DFT within the Perdew–Burke–Ernzerhof generalized gradient approximation,[6-10] as implemented in the CASTEP package of Materials Studio 6.0. The final set of energies was computed using an energy cutoff of 400 eV for all calculations. Geometry optimization was performed using a 4 × 4 × 1 supercell containing 18 C atoms. All atoms were fully relaxed until the residual forces on each atom decreased to <0.02 meVÅ^{-1}. The diffusion barrier calculations of PF_6 were considered in the model construction of anion-intercalated graphene [PF_6 $C_{63}B$)] and were performed using the linear synchronous transit/quadratic synchronous transit (LST/QST) method. The Brillouin zone integration was performed using the 3 × 3 × 2 and 1 × 1 × 1 Γ-centered Monkhorst-Pack k-point meshes in geometry optimization and LST/QST calculations, respectively.

Supplementary Figures

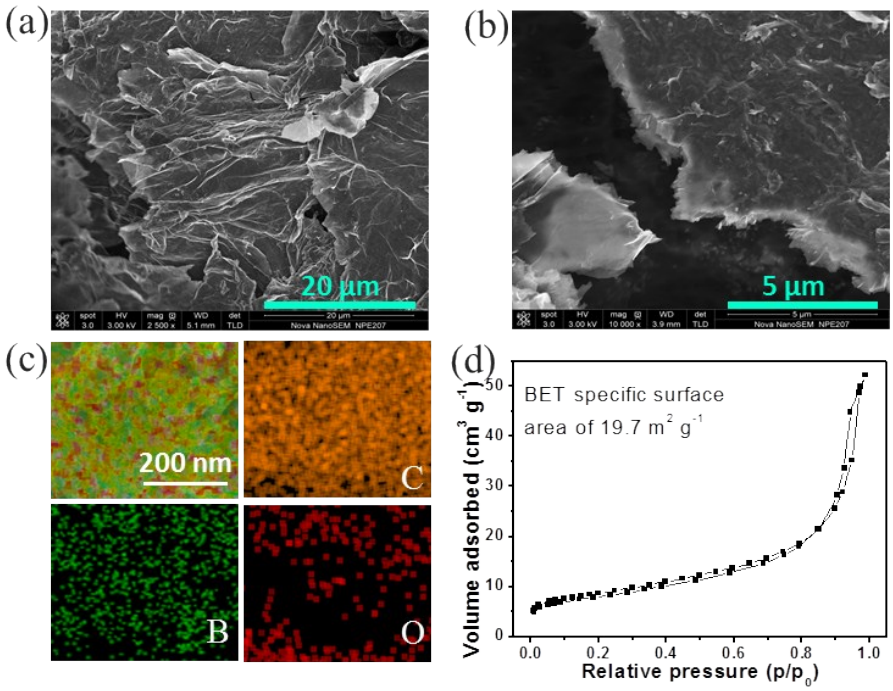

Supplementary Fig. S1 (a, b) SEM images and (c) EDX mapping of the BG sample. The BG sample exhibited the sheet-like morphology with micron-level size. (d) The nitrogen adsorption-desorption isotherm of BG sample with a BET specific surface area of 19.7 m^2 g^{-1}.

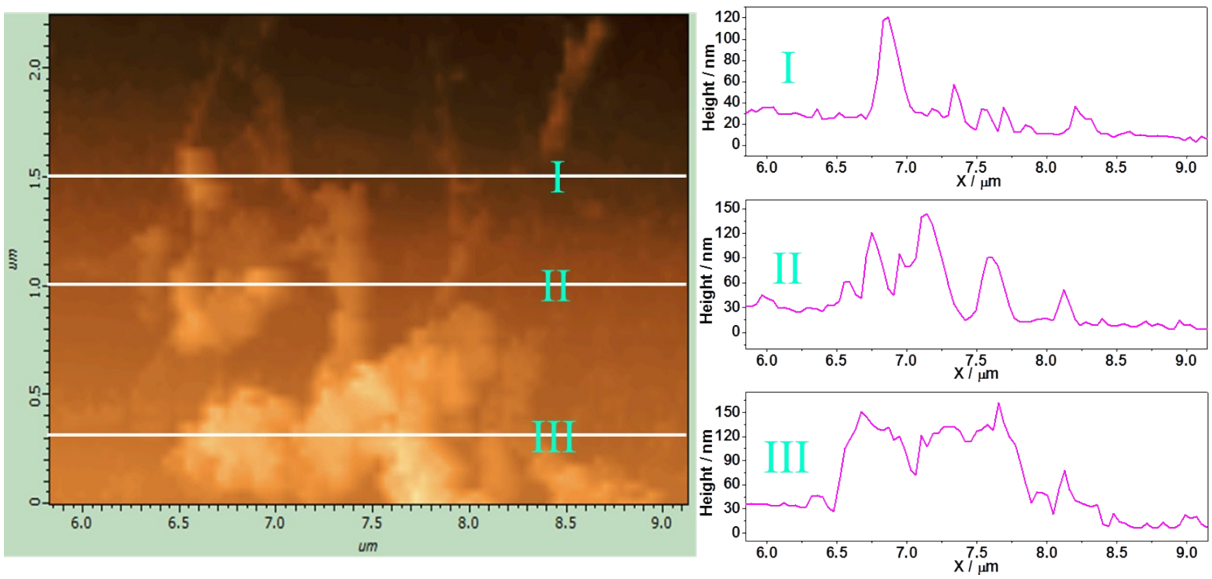

Supplementary Fig. S2 AFM image and the corresponding thickness of BG.

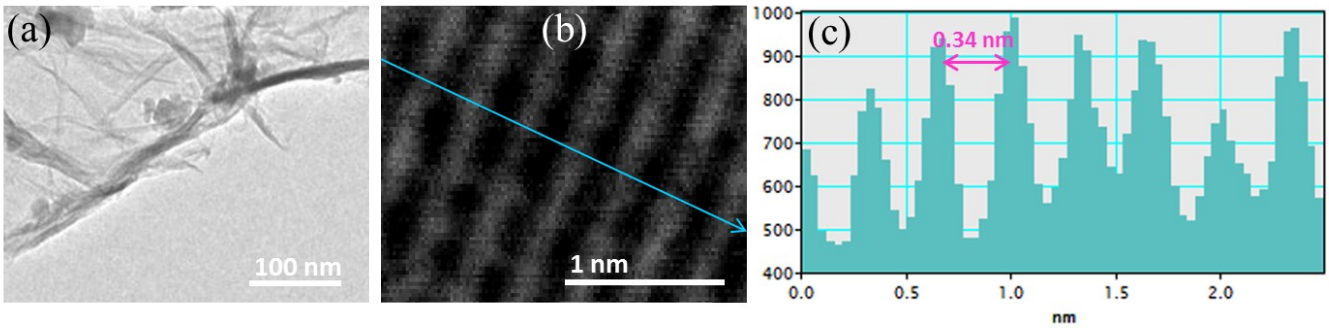

Supplementary Fig. S3 (a, b) TEM images and (c) the corresponding lattice spacing of BG sheets.

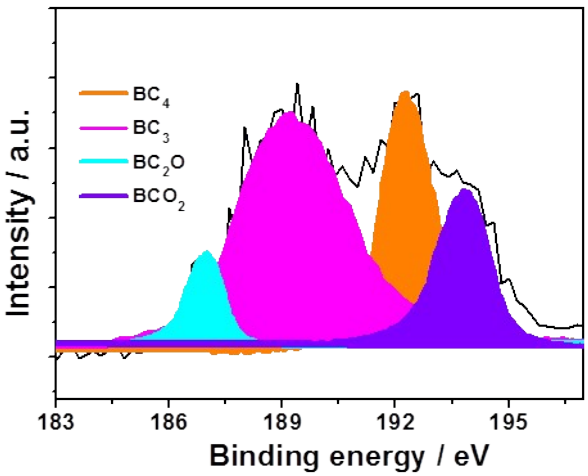

Supplementary Fig. S4 the XPS spectrum of B_{1s} peak for the BG sheet.

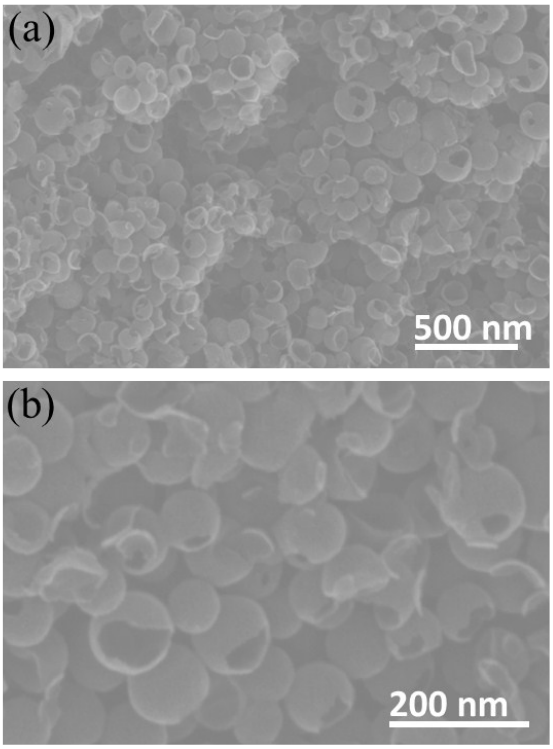

Supplementary Fig. S5 (a, b) SEM images of the HC with some cracking parts.

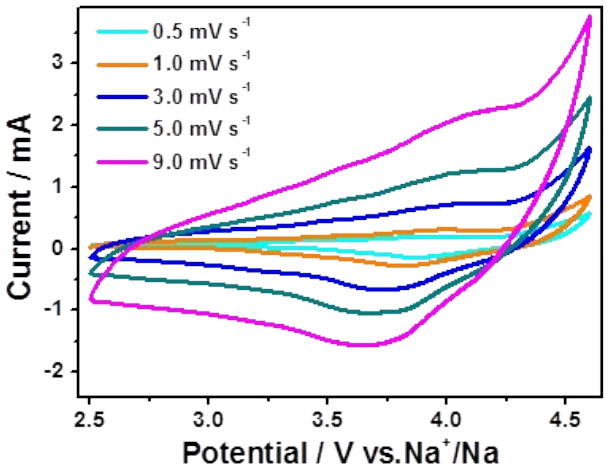

Supplementary Fig. S6 Cyclic voltammetry (CV) curves of the BG electrode at various sweep rates.

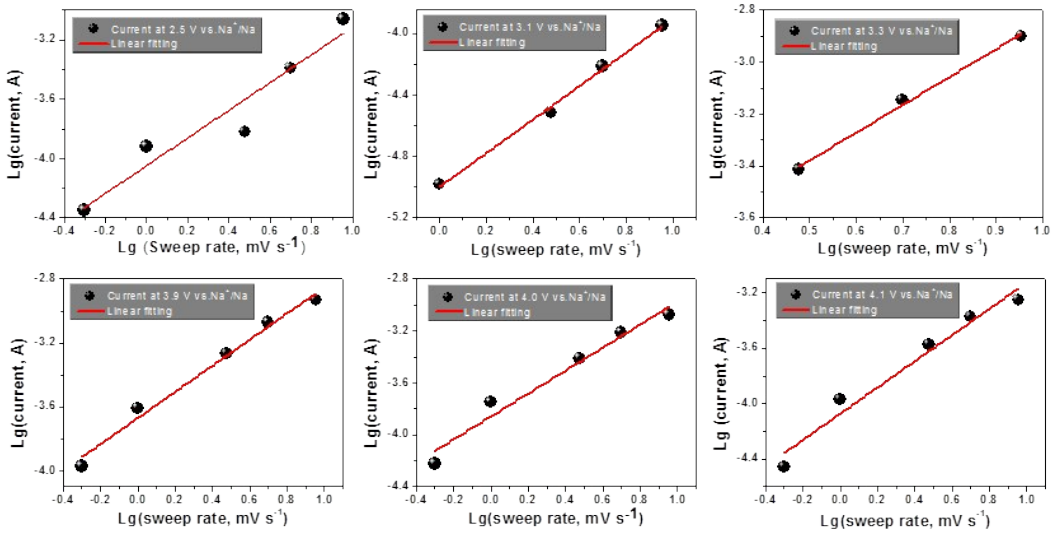

Supplementary Fig. S7 The determination of *b* values at various potentials.

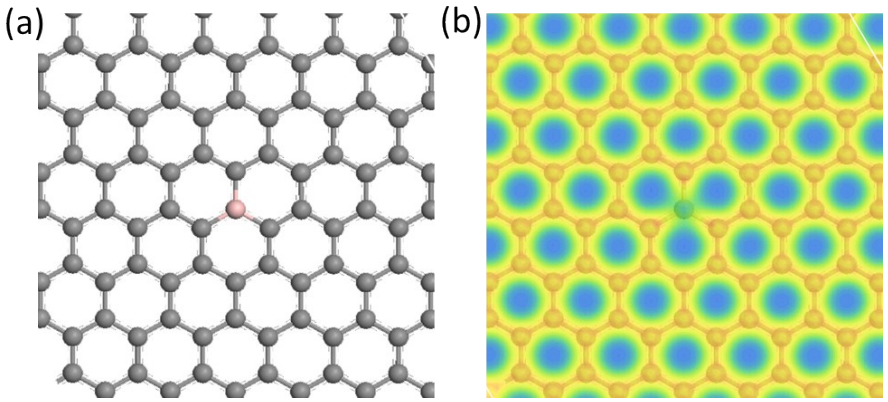

Supplementary Fig. S8 (a) The structure and (b) the charge density for B-doped graphite layer.

The calculated charge density reveals the B atom with remarkably lower charge density relative to C atoms. This means that the B atom with electropositivity tends to attract PF_6^- ions with electronegativity more easily than C atoms. In other words, the electrostatic potential distribution of B-doped graphite layer has been significantly changed and their combination with PF_6^- ions would be influenced.

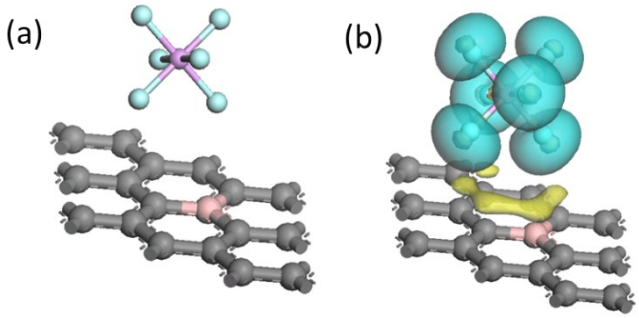

Supplementary Fig. S9 (a) The optimized configurations and (b) the colour-filled reduced density gradient (RDG) isosurfaces (e) for the surface interaction of PF_6^- ions with the B-doped graphite layer. The yellow and blue regions indicate an increase and decrease in electron density, respectively.

To prove the prediction in Fig. S8, the interaction configurations of PF_6^- ions at highly probable interaction sites identified from the density functional theory calculations were shown in Fig. S9 (a). It could be seen that the interaction sites were close to the B-C site consistent with the above prediction. From the color-filled RDG (reduced density gradient) isosurfaces (Fig. S9b),[11,12] there is a large charge deficiency at B-C and charge excess around nearby PF_6 atoms. Such strong electron transfer from PF_6^- ions to phosphorene indicates a p-typed chemical reaction between anion and B-doped graphite sheets.

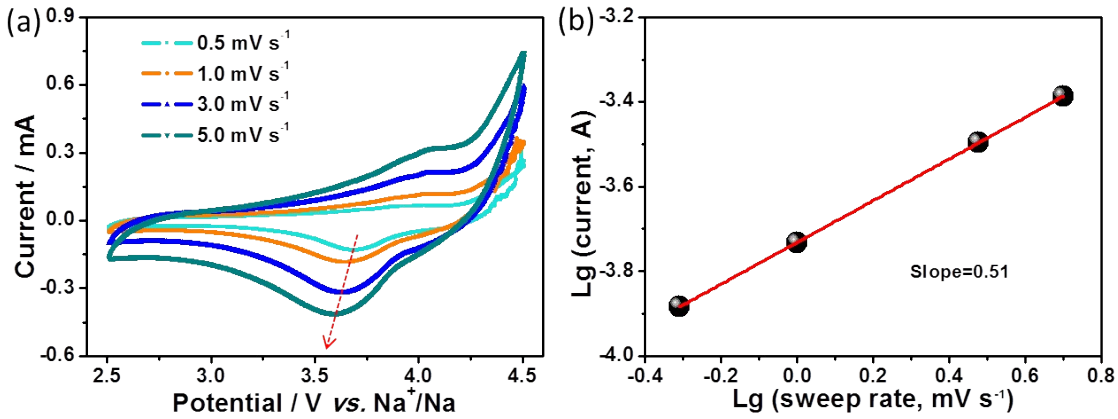

Supplementary Fig. S10 (a) CV curves of pure graphite electrode at various sweep rates. (b) The determination of the *b*-value at cathodic peak regimes.

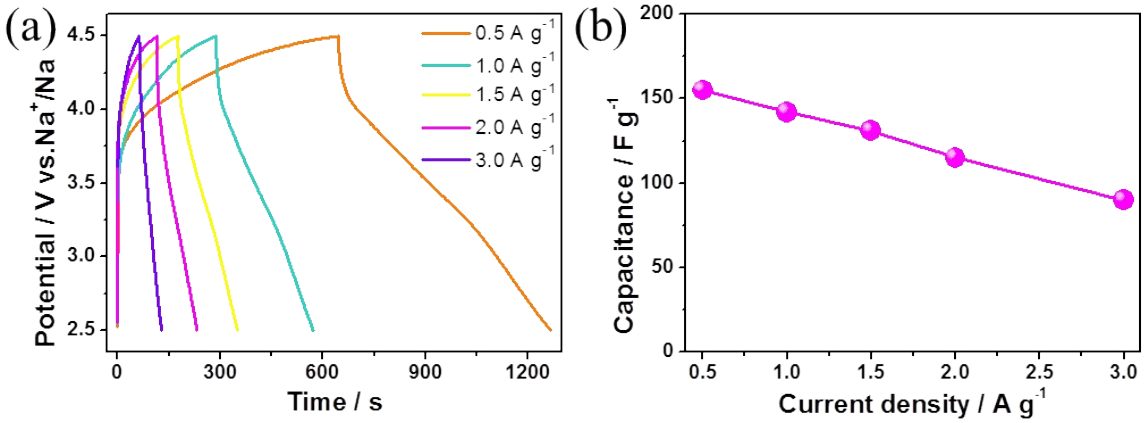

Supplementary Fig. S11 (a) Galvanostatic charge/discharge curves and (b) specific capacitances of BG electrode at various current densities.

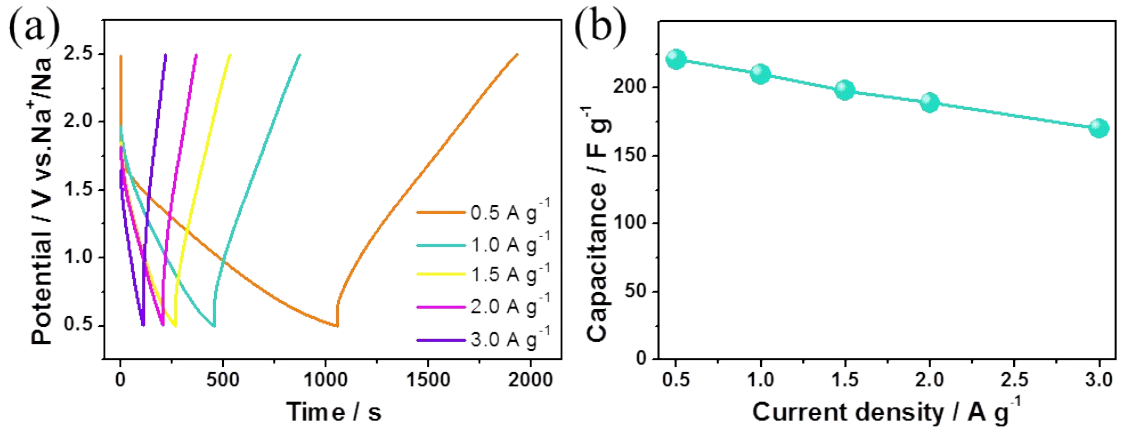

Supplementary Fig. S12 (a) Galvanostatic charge/discharge curves and (b) specific capacitances of HC electrode at various current densities.

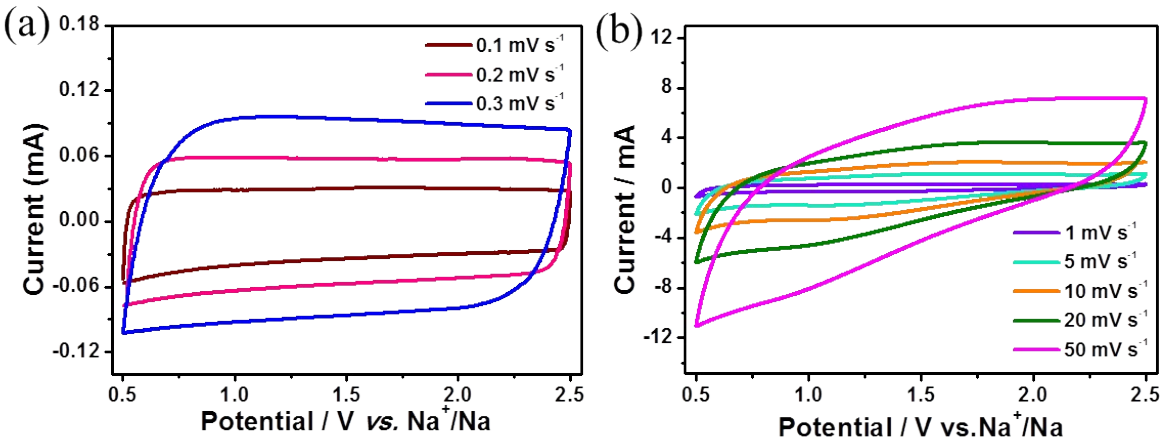

Supplementary Fig. S13 (a) Cyclic voltammetry (CV) curves of hollow carbon (HG) electrode at various sweep rates. The CV curves were collected after the initial CV cycle (activation) at 0.1 mV s^{-1}.

All CV curves from 0.1 mV s^{-1} to 0.3 mV s^{-1} exhibited rectangular shapes (Fig. S13a). At large sweep rates, the CV curves are distorted from rectangular shape to a certain degree (Fig. S13b). Anyway, the ionic conductivity of the used organic electrolytes (1 M $NaPF_6$ in ethylene carbonate/dimethyl carbonate) is about two orders of magnitudes lower than that of aqueous electrolytes. Thus, the CV curves of HC electrode in this organic electrolyte cannot achieve perfect rectangular shape in aqueous electrolyte at large sweep rate. Even so, it is still reasonable to call the HC electrode as EDLC-type electrode.

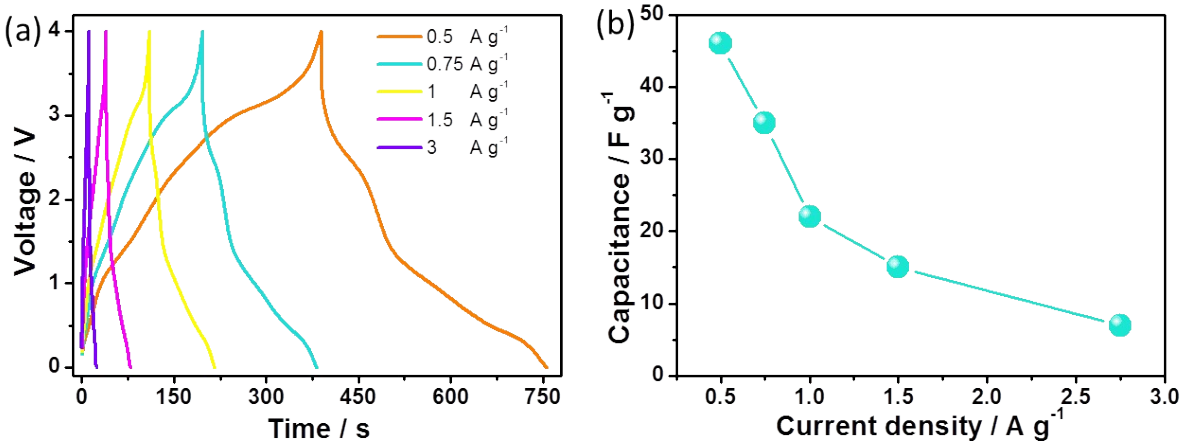

Supplementary Fig. S14 (a) Galvanostatic charge/discharge curves and (b) the related specific capacitances *vs.* current densities of the fabricated Na-ion hybrid capacitor based on un-doped graphite sheets as cathode (with diffusion-controlled kinetics) and the anode (HC anode with EDL typed surface-controlled kinetics).

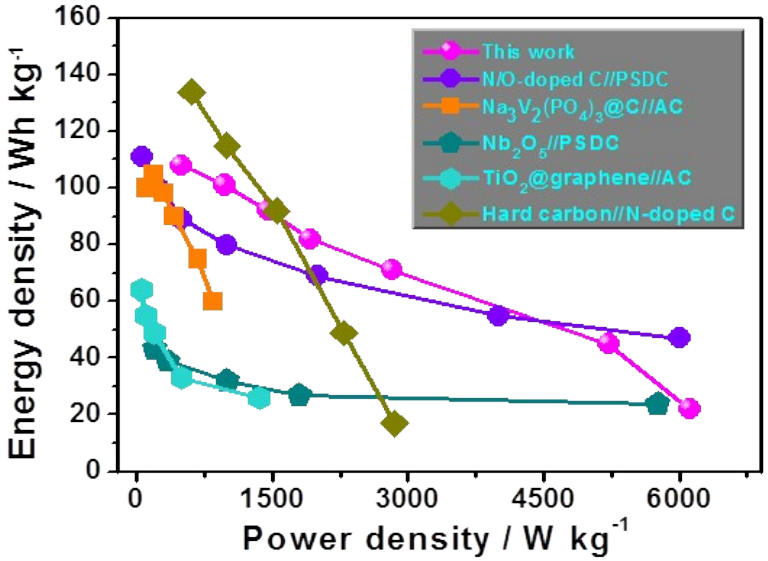

Supplementary Fig. S15 The energy and power densities of this Na-ion hybrid capacitor compared with advanced metal-ion hybrid capacitors, involving N/O-doped C//PSDC (*Nano Energy, 2016, 23, 129*), $Na_3V_2(PO_4)_3$@C//AC (*Adv. Energy Mater. 2016, 6, 1502199*), Nb_2O_5//PSDC (*Chem. Mater. 2016, 28, 5753*), hard carbon//N-doped C (*Nano Energy 2017, 41, 674*) and TiO_2@graphene//AC (*ACS Nano 2017, 11, 2952*).

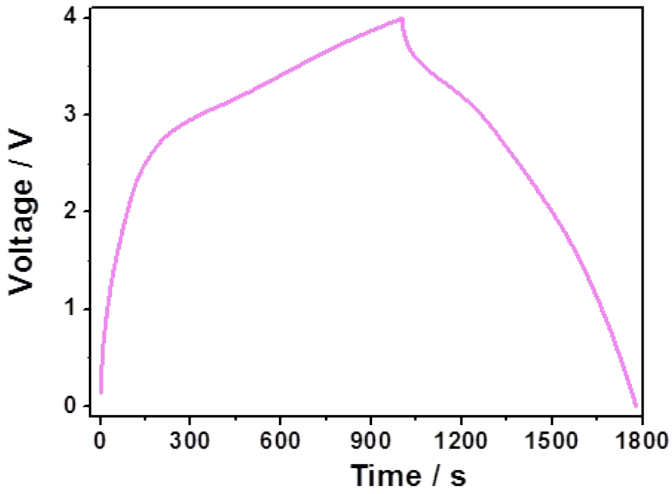

Supplementary Fig. S16 The initial charge/discharge curves of the Na-ion hybrid capacitor at 0.25 A g^{-1}.

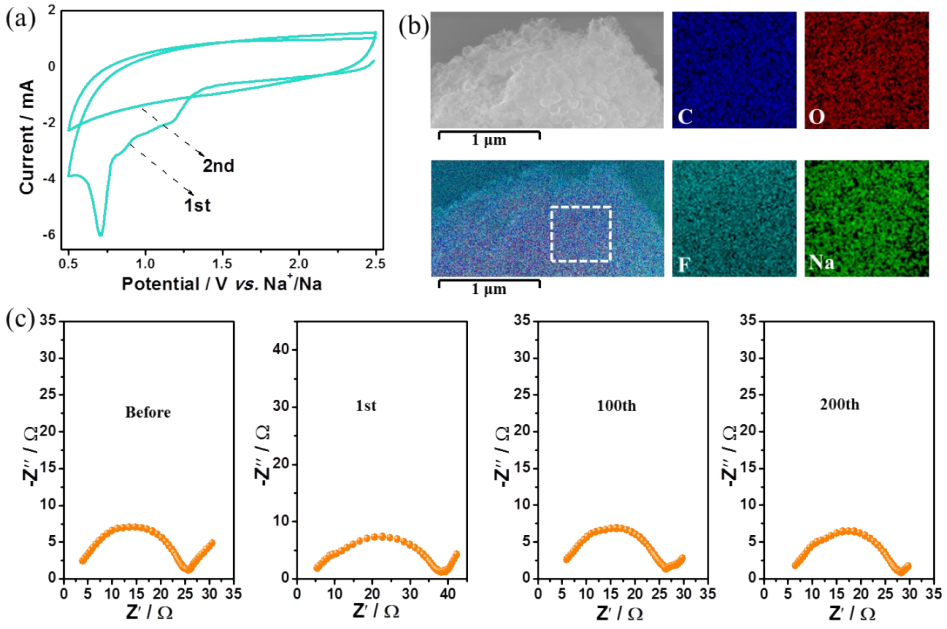

Supplementary Fig. S17 (a) The initial two cycles of the anode in half cell. (b) The SEM images and the related elemental mappings in the dotted square area after 100 cycles. (c) The Nyquist plots of the fabricated Na-ion hybrid capacitor at various cycling states.

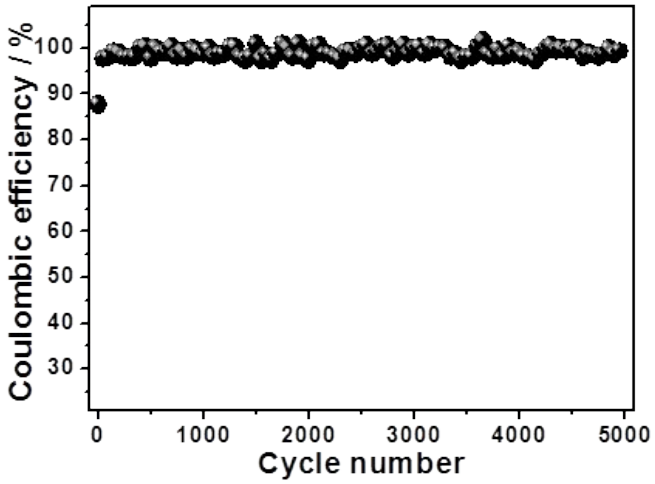

Supplementary Fig. S18 The coulombic efficiency of the Na-ion hybrid capacitor during repeated charge/discharge cycles at 1 A g^{-1}.

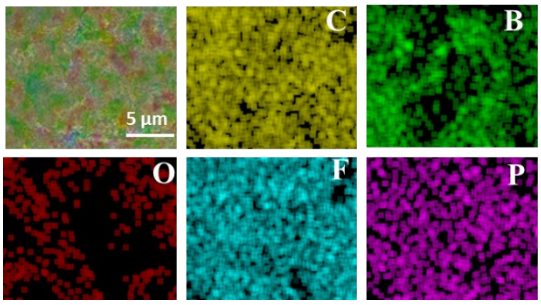

Supplementary Fig. S19 SEM elemental mappings for the BG electrode after charging to 4 V.

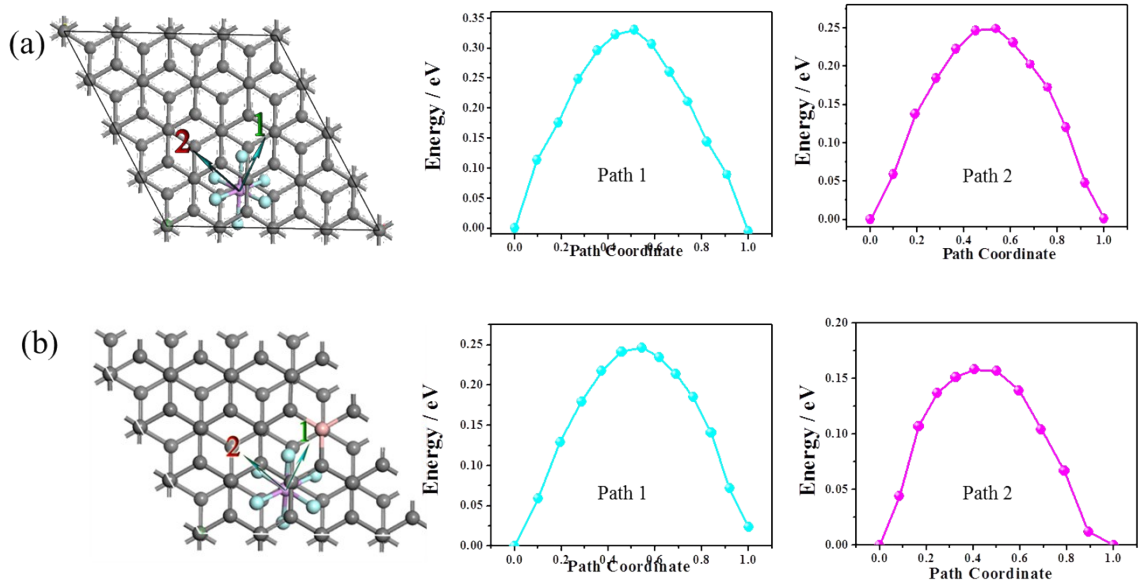

Supplementary Fig. S20. The PF_6 diffusion and the corresponding energy barriers along (010) (path 1) and (011) (path 2) directions in (a) graphite layers and (b) B-doped graphite layers.

Table S1 The state-of-the-art electrochemical performance of the reported Na ion hybrid capacitor during the past three years and the Na ion hybrid capacitor with anion intercalation pseudocapacitance in this work.

Type	**Electrode material (-)//(+)**	**Maximum energy density / Wh kg^{-1}**	**Maximum power density / W kg^{-1}**	**Cycle**	**Reference**
Negative electrode: Na-ion Faradaic or pseudocapacitive redox reaction. **Positive electrode:** anion EDLC	Hard carbon//graphene	160	2800	1200 (85%)	*Adv. Mater.* **2015**, *27*, 6962.
	Ti_2C//$Na_2Fe_2(SO_4)_3$	260[a]	14000[a]	100 (99%)	*Nat. Commun.* **2015**, *6*, 6544.
	Hard carbon//V_2C	85	-	300 (70%)	*J. Phys. Chem. Lett.* **2015**, 6, 2305.
	N/O-doped C//PSDC	111	14500	5000 (86%)	*Nano Energy* **2016**, *23*, 129.
	$Na_3V_2(PO_4)_3$@C//AC	118	900	10000 (95%)	*Adv. Energy Mater.* **2016**, *6*, 1502199.
	Nb_2O_5//PSDC	43	5670	3000 (80%)	*Chem. Mater.* **2016**, *28*, 5753.
	Nb_2O_5@C//graphene	76	20800	3000 (80%)	*Adv. Funct. Mater.* **2016**, *26*, 3711.
	$Na_2Ti_3O_7$//PSDC	111	11200	3000 (86%)	*Nano Lett.* **2016**, *16*, 5938.
	Hard carbon//N-doped C	157	2400	1000 (70%)	*Nano Energy* **2017**, *41*, 674.
	TiO_2@CNT@C//AC	81	12400	5000 (85%)	*Adv. Energy Mater.* **2017**, DOI: 10.1002/aenm.201701222.
	TiO_2@graphene//AC	64	1357	10000 (90%)	*ACS Nano* **2017**, *11*, 2952.
Negative electrode: Na-ion EDLC **Positive electrode:** anion intercalation + pseudocapacitive reaction	Hollow C//B-doped graphite nanosheets	108	6200	5000 (97%)	This work

PSDC: peanut shell derived carbon AC: Activated carbon

[a] The value is just based on the mass of negative electrode

References

1 S. Yang, S. Brüller, Z. S. Wu, Z. Liu, K. Parvez, R. Dong, F. Richard, P. Samorì, X. Feng and K. Müllen, *J. Am. Chem. Soc.*, 2015, **137**, 13927−13932.

2 C. Wang, F. Wang, Z. Liu, Y. Zhao, Y. Liua, Q. Yue, H. Zhu, Y. Deng, Y. Wu and D. Zhao, Nano Energy, 2017, **41**, 674–680.

3 F. Wang, C. Wang, Y. Zhao, Z. Liu, Z. Chang, L. Fu, Y. Zhu, Y. Wu and D. Zhao, *Small*, 2016, **12**, 6207–6213.

4 E. Lim, C. Jo, M. S. Kim, M. H. Kim, J. Chun, H. Kim, J. Park, K. C. Roh, K. Kang, S. Yoon and J. Lee, *Adv. Funct. Mater.*, 2016, **26**, 3711–3719.

5 H. Li, Y. Zhu, S. Dong, L. Shen, Z. Chen, X. Zhang and G. Yu, *Chem. Mater.*, 2016, **28**, 5753−5760.

6 P. E. Blochl, *Phy. Rev. B.* 1994, **50**, 17953–17979.

7 X. Wang, R. Xiao, H. Li and L. Chen, *Phys. Rev. Lett.*, 2017, **118**, 195901–195906.

8 J. P. Perdew, K. Burke and M. Ernzerhof, *Phys. Rev. Lett.*, 1996, **77**, 3865–3868.

9 W. Lei, V. N. Mochalin, D. Liu, S. Qin, Y. Gogotsi and Y. Chen, *Nat. Commun.*, 2015, **6**, 8849–8857.

10 W. J. Li, J. Liu, Z. H. Sun, T. F. Liu, L. Jian, S. Y. Gao, C. He, R. Cao and J. H. Luo, *Nat. Commun.,* 2016, **7**, 11830–11838.

11 Q. Yao, C. Huang, Y. Yuan, Y. Liu, S. Liu, K. Deng and E. Kan, *J. Phys. Chem. C*, 2015, **119**, 6923−6928.

12 G. C. Guo, D. Wang, X. L. Wei, Q. Zhang, H. Liu, W. M. Lau and L. M. Liu, *J. Phys. Chem. Lett.*, 2015, **6**, 5002−5008.